Actomyosin remodeling regulates biomineral formation, growth and morphology during eukaryote skeletogenesis

Eman Hijaze[1], Tsvia Gildor[1], Ronald Seidel[2], Mark Winter[3], Luca Bertinetti[2], Majed Layous[1], Yael Politi[2] and Smadar Ben-Tabou de-Leon[1,*]

[1]Department of Marine Biology, Leon H. Charney School of Marine Sciences, University of Haifa, Haifa 31905, Israel.

[2]B CUBE Center for Molecular Bioengineering, Technische Universität Dresden, 01309 Dresden, Germany.

[3]Department of Electrical Engineering, Computer Science and Mathematics, Technische Universiteit Delft, Delft 2628CD, Netherlands

*Correspondence: Smadar Ben-Tabou de-Leon (sben-tab@univ.haifa.ac.il)

Abstract

Biomineralization, the ability of organisms to use minerals to harden their tissues, has attracted scientists from various disciplines to decipher the molecular mechanisms that control it. Many of these studies focus on the gene regulatory networks (GRNs) that control biomineralization and are apparently, phylum specific. Yet, downstream to the GRNs lays the cellular machinery that drives morphogenetic processes that are commonly used in biomineralization, such as, vesicular motion and secretion. The actomyosin network is a key regulator of these processes and participates in biomineralization across Eukaryotes, from unicellular organisms to vertebrates, yet, little is known about its regulation of biomineral growth. Here we reveal that the actomyosin remodeling protein, Rho-associated coiled-coil kinase (ROCK), controls the formation, growth and morphology of the calcite spicules in the sea urchin larva. We show that ROCK expression is elevated in the sea urchin skeletogenic cells and its inhibition impairs the organization of F-actin around the spicules and leads to skeletal loss. We discovered that ROCK inhibition after spicule formation, slows down mineral deposition, induces ectopic spicule branching and disrupts skeletogenic gene expression. We propose that ROCK and the actomyosin network are an essential part of the common biomineralization tool-kit in Eukaryotes.

Key words: Biomineralization, Sea urchin, ROCK, Actomyosin network, Skeletogenesis,

Introduction

Biomineralization is the process in which organisms from the five kingdoms of life, use minerals to produce shells, skeletons and teeth that protect and support them [1-9]. Recent studies suggest that biomineralization evolved by the phylum specific co-option of ancestral gene regulatory networks (GRNs) that drove the construction of distinct organic scaffolds [3, 5, 6, 9-12] and by the evolution of specialized sets of biomineralization proteins [1-3, 8, 11, 13-15]. This explanation is in line with the dissimilar GRNs and biomineralization proteins that drive biomineralization in different phyla [2, 5, 16]. Yet, there are common cellular processes required for mineralization in highly diverse phyla [9], suggesting that distinct upstream GRNs might have recruited common molecular mechanisms to drive biomineralization.

A shared design of the mineral pathway across different calcifying phyla, is the role of mineral bearing vesicles, their trafficking and deposition into a dedicated biomineralization compartment [4, 9, 17-19]. In vertebrates, the biomineralizing cells, chondrocytes, osteoblasts and odontoblasts, secret matrix vesicles containing biomineralization enzymes and hydroxyapatite, that are the initial site of mineral nucleation [20, 21]. Vesicular trafficking and localized deposition are controlled in many systems by the activity of actomyosin networks formed by actin filaments (F-actin), non-muscle myosin II (MyoII), and actomyosin remodeling proteins such as the Rho family GTPases, RhoA, CDC42 and Rac [22-28]. The actomyosin network was shown to play a role in biomineralization in various Eukaryote models, from unicellular organisms to vertebrates' bones and teeth [20, 29-35]. Specifically, vertebrates' Rho GTPases and Rho-associated coiled-coil kinase (ROCK) regulate chondrocytes, osteoblasts and odontoblasts differentiation and affect genes expression in these biomineralizing cells [20, 34, 35] However, the roles of actomyosin remodeling in controlling mineral deposition and shaping biomineral morphology, are still unclear.

Sea urchin larval skeletogenesis provides an attractive model to study the role of the actomyosin network in biomineralization. Sea urchin larval skeletons are made of two frameworks of interconnected calcite rods, termed "spicules" that are generated by the skeletogenic cells [6, 36]. To make the spicules, the skeletogenic cells form a ring with two

lateral skeletogenic clusters and fuse through their filopodia forming a pseudopodia cable that links them into a syncytium [37, 38]. The mineral is concentrated in the form of amorphous calcium carbonate (ACC) inside intracellular vesicles [19]. The vesicles are secreted into the biomineralization compartment generated in the skeletogenic cell clusters forming two triradiate spicules (Fig. 8A, [19, 39]). The tubular biomineralization compartment, also called the spicule cavity, elongates within the pseudopodia cable by localized mineral deposition at the tip of each rod [40].

The GRN that controls sea urchin skeletogenesis is known in great detail and shows remarkable similarity to the GRN that controls vertebrates' vascularization, suggesting a common evolutionary origin of these two tubulogenesis programs [6, 36, 41, 42]. As the spicules elongate, the expression of key regulatory and biomineralization related genes becomes restricted to the skeletogenic cells proximal to the growing tips, possibly to promote mineral deposition at these sites [43-45]. Localized gene expression is regulated by signaling cues such as the Vascular Endothelial Growth Factor (VEGF) signaling [43, 44]. However, how the skeletogenic GRN drives spicule formation and localized mineral deposition at the tips of the rods is poorly understood.

Previous works suggest that the actomyosin network is essential for skeletal growth and could be regulating mineral deposition. Calcium bearing vesicles perform an active diffusion motion in the skeletogenic cells with a diffusion length that inversely correlates with the strength and activity of the actomyosin network [46]. Actin filaments are formed around the spicule [46, 47] and F-actin signal is enriched at the tips of the growing skeletal rods in skeletogenic cell culture [48]. Genetic and pharmacological perturbations of the GTPase, CDC42, prevent the formation of filopodia in the skeletogenic cells and inhibit spicule formation and elongation [49]. Pharmacological perturbations of ROCK prevent spicule formation [50] and genetic perturbations of Rhogap24l/2 result with ectopic spicule splitting [6]. Despite these phenotypic characterizations, little is known on the regulation and role of the actomyosin network and remodeling proteins in localized mineral deposition.

Here we study the spatiotemporal pattern of ROCK expression, investigate the role of ROCK in mineral uptake and deposition, study the role of ROCK and the actomyosin

network in skeletal growth and morphology and investigate the effect of ROCK inhibition on skeletogenic gene expression, in the sea urchin *Paracentraorus lividus (P. lividus)*. Our findings reveal the critical role of ROCK and the actomyosin network in multiple aspects of sea urchin biomineralization, suggesting a common use of the actomyosin network in Eukaryote biomineralization, downstream of distinct GRNs.

Results

ROCK is enriched in the skeletogenic cells, partially depending on VEGF signaling

We sought to study the expression and cellular localization of the ROCK protein and its regulation by VEGF signaling, a prominent regulator of sea urchin skeletogenesis [6, 41, 42]. The sequence of ROCK and especially, its functional domains are highly conserved between human and sea urchin (Fig. S1). We therefore used a commercial antibody that recognizes human ROCK protein to test ROCK expression in *P. lividus* embryos (Fig. S2). We first extracted proteins from whole embryos and used western blot to detect ROCK expression in control and under VEGFR inhibition at the time of spicule formation and during skeletal elongation (~22 hours post fertilization [hpf], 27hpf and 33hpf, Fig. S2). The antibody detected a ~150kDa protein (Fig. S2A) that is the predicted size for *P. lividus* ROCK protein (153kDa). VEGF inhibition did not affect the overall level of ROCK in at the three time points we tested (Fig. S2B). Yet, this measurement was done on proteins extracted from whole embryos, and we wanted to study the spatial expression of ROCK and its regulation in the skeletogenic cells.

We studied the spatial distribution of ROCK protein within the sea urchin embryo, using ROCK antibody and the skeletal marker, 6a9, that marks the skeletogenic syncytium membrane ([51], Fig. 1). We quantified ROCK signal in the skeletogenic cells compared to the neighboring ectodermal cells in control embryos and under VEGFR inhibition, at the three time points mentioned above. At 22hpf, ROCK expression in the skeletogenic cells is mildly elevated compared to the neighboring ectodermal cells and ROCK enrichment is not observed under VEGFR inhibition (Fig. 1A-F). At 27hpf, ROCK enrichment in the skeletogenic cells increases, but similar enrichment is observed under VEGFR inhibition, indicating that VEGF signaling is not responsible for ROCK skeletogenic enrichment at this stage (Fig. 1G-L). At 33hpf, ROCK enrichment in the skeletogenic cells is most

apparent (Fig. 1M-O). A much weaker skeletogenic enrichment is observed under VEGFR inhibition, suggesting that continuous VEGF signaling is required for ROCK upregulation in the skeletogenic cells (Fig. 1P-S, average ratio of 4.6 compared to 1.5). At both 27hpf and 33hpf in control embryos, ROCK seems localized near the skeletogenic cell membranes, which further supports its activation in these cells, since in other systems ROCK activation leads to its localization to the cell membranes [52]. Overall, our studies demonstrate that ROCK expression is elevated in the skeletogenic cells and this enrichment strengthens with skeletal elongation and partially depends on VEGF signaling.

ROCK activity controls spicule initiation, growth and morphology

Next, we studied the role of ROCK in sea urchin skeletogenesis using genetic perturbations. We downregulated the expression of ROCK by the injection of two different morpholino anti-sense oligonucleotides (MASOs) that block the translation of the gene at two different regions. ROCK MASO-1 matches the start of translation region, ROCK MASO-2 matches the 5' region upstream the start of translation, and random MASO was used as a control (see methods for details). The two ROCK MASOs induced substantial skeletogenic phenotypes compared to the control MASO (Fig. 2A-E). Embryos injected with either ROCK MASO-1 or MASO-2 show strongly reduced skeletons (Fig. 2C, D) and embryos injected with ROCK MASO-2 show an additional phenotype of severely branched skeleton (Fig. 2B). The additional branching phenotype and the larger percentage of affected embryos in ROCK MASO-2 are probably due to its higher efficiency resulting from its more 5' location relative to translation start codon (Fig. 2E). Thus, the genetic perturbations of ROCK expression indicate that sea urchin ROCK is important for skeletal elongation and normal branching.

To elucidate the dosage dependence of ROCK activity and identify its effect on different stages of skeletogenesis, we tested the skeletogenic phenotypes of different concentrations of ROCK inhibitor, Y27632, applied before or after spicule initiation (Fig. 2F, see methods for details). Y27632 binds to the ATP site of ROCK's kinase domain and prevents its activity [53]. The amino-acids to which Y27632 binds, are conserved in the sea urchin ROCK protein, supporting its specific inhibition of this protein (Fig. S1C).

The concentration and timing of ROCK inhibition leads to diverse skeletogenic phenotypes suggesting multiple roles of ROCK activity in sea urchin skeletogenesis (Fig. 2G-P, S3). Continuous ROCK inhibition, beginning at egg fertilization, using 80µM Y27632, did not affect skeletogenic cell migration but eliminated skeletal formation at 27hpf (Fig. 2G, H). At two days post fertilization (dpf) the majority of the embryos completely lack skeleton and the rest show only spicule initiations, yet their overall embryonic development seems normal (Fig. 2J, P, in agreement with [50]). Similar results are observed when adding the inhibitor in this concentration at 20hpf (Fig. 2K, P). Yet, the addition of 80µM of the inhibitor at 25hpf, after spicule initiation, results in a majority of embryos with severe ectopic spicule branching, which resembles the branching phenotype observed in ROCK MASO-2 (Fig. 2L, P). Reducing the concentration of the added inhibitor leads to milder branching and elongation phenotypes (Fig. 2M, N, P, S2). However, even at the lowest inhibitor concentration, we detect a reduction of skeletal growth rate and ectopic branching a few hours after the addition of ROCK inhibitor (Fig. S4, 30µM). Washing the inhibitor after 25hpf results in partial recovery of skeletogenesis, with normal or mildly delayed skeletons (Fig. 2O, P, S3). Overall, our genetic and pharmacological perturbations indicate that ROCK activity is necessary for spicule formation, skeletal elongation and normal branching pattern.

ROCK inhibition reduces spicule volume, surface area and total length, but not thickness (SR-µCT)

To quantify the effect of ROCK inhibition on mineral deposition and skeletal shape we used synchrotron radiation micro-computed tomography (SR-µCT) that enables three-dimensional visualization and quantification of spicule morphology at 2 and 3dpf (Figs. 3, S5, see methods for details). The aberrant morphology of ROCK inhibited spicules is visible at both developmental time points (Fig. 3A). The ectopic branching occurs both at the tips, where we observe tip-splitting (arrowheads, Fig. 3A), as well as in the back, where we observe small spicule extensions, or spicule ‘dripping’ (arrow at 48hpf, Fig. 3A). This implies that the localization of mineral deposition is perturbed both at the tip and in the back of the spicules under ROCK inhibition.

When compared to control spicules, ROCK inhibition leads to a ~2.5-fold reduction of the spicule volume and surface area in both 2 and 3dpf (Fig. 3B-D): The mean volume of control spicules at 2dpf is 6,850 μm^3±2,000 μm^3 compared to 2,925 μm^3±974 μm^3 under ROCK inhibition. The mean volume of the spicules at 3dpf is 14,673 μm^3±2,747 μm^3, compared to 5800 μm^3±2409 μm^3 in ROCK inhibition (see Table S2 for details and S3 for statistical analyses). Similar trends were measured for surface area (2dpf control, 5823μm^2±1122μm^2, ROCK inhibition, 2335μm^2±607µm2; and 3dpf control, 9897μm^2±1200 μm^2, ROCK-inhibition, 4003μm^2±1250μm^2. See tables S2 and S3). These SR-µCT measurements show that the rate of mineral deposition is significantly reduced under ROCK inhibition.

To understand the specific effect of ROCK inhibition on spicule elongation vs. thickening, we compared the total length and the mean thickness of the spicules between control and ROCK inhibition (Fig. 3E-G). The total length of control spicules was on average about 2.5-times longer than the length under ROCK inhibition in both 2dpf and 3dpf (2dpf control: 497µm±62µm, ROCK inhibition: 188µm±50 µm; and 3dpf control: 697µm±71µm, ROCK inhibition: 276µm±81µm. Fig. 3E, F, tables S2 and S3). In contrast to its effect on the spicule length, ROCK inhibition lead to a minor increase of the spicule thickness at 2dpf, that is statistically significant (2dpf control: 3.7µm±1.4µm, ROCK inhibition: 3.9µm±1.6 µm). At 3dpf the thickness was not affected by the inhibition (3dpf control: 4.4µm±2 µm, ROCK inhibition: 4.4µm±1.7 µm, Fig. 3E, G, Table S2, S3). These SR-µCT measurements indicate that ROCK activity plays a crucial role in controlling the localization and rate of mineral deposition at the tips of the rods and preventing ectopic spicule branching at the tips and in the back of the spicules.

ROCK activity does not control mineral uptake but is required for "tip-dominance"

To test the effect of ROCK inhibition on mineral intake, we used the fluorescent chromophore, calcein that binds to divalent ions including Ca^{+2} and is widely used to track the calcium pathway in biomineralization [6, 39, 45, 46]. We measured the number of calcium vesicles per area as well as the number of pixels of calcein signal per area in the skeletogenic cells, in control and under ROCK inhibition at 1dpf and 2dpf (Fig. S6A-E). Continuous ROCK inhibition does not change the number of calcium bearing vesicles at

1dpf, but the number of calcein stained pixels significantly increases in this condition, possibly indicting that the vesicle volume is larger (Fig. S6F, G). At 2dpf, the number of calcein stained pixels is similar in control and in continuous ROCK inhibition, suggesting that the overall calcium content does not change in this condition (Fig. S6H, I). The number of calcein stained vesicles is decreased under ROCK inhibition, possibly indicating that there are fewer vesicles with larger volume. Addition of ROCK inhibitor at 25hpf affects neither the number of calcein stained vesicles nor the number of calcein stained pixels in the skeletogenic cells. Together, these measurements show that ROCK is not required for the uptake of calcium into the cells. Therefore, the skeletal phenotypes occurring under ROCK inhibition are not related to a decrease in calcium uptake or shortage in intracellular calcium.

To monitor the effect of ROCK inhibition on mineral deposition rate and distribution, we applied two pulses of different calcein dyes: blue calcein was added at 29hpf and washed after one hour, followed by green calcein added at 44hpf and washed after one hour. Hence, blue calcein marks the initial triradiate region and green calcein marks the edges of the spicules that were recently deposited (blue and green arrows in Fig. 3H, I). The dye FM4-64 was used to mark the cell membranes. Under ROCK inhibition, the green labeled region is much closer to the blue labeled region compared to control, due to the reduction in skeletal elongation rate, in agreement with our SR-µCT measurements. However, while in control embryos each body rod has a single tip stained in green calcein, under ROCK inhibition one of the body rods has two tips and both are stained in green. This indicates that mineral is being deposited in both edges, and the mechanism that prevents the growth of multiple tips in each rod, enabling “tip-dominance”, is disrupted under ROCK inhibition.

F-actin is essential for normal spicule elongation and inhibition of ectopic branching

In other systems, major roles of ROCK are to control F-actin stabilization and MyoII activation [22, 54-57], hence we wanted to directly test the role of these actomyosin components in sea urchin skeletogenesis. To directly inhibit F-actin polymerization we used Latrunculin-A (Lat-A), that prevents the polymerization of actin monomers [58] and was shown to be effective in sea urchin embryos [59]. To directly inhibit actomyosin contractility we used Blebbistatin (Blebb), that interferes with MyoII ATPase activity,

prevents actin-myosin interactions [60] and was shown to be effective in sea urchin embryos [61]. To prevent interference with the early cell divisions where the actomyosin network plays a critical role [62-64], we added the inhibitors, individually or together, before or after spicule formation (20hpf and 25hpf, Fig. 4A, see methods for details). We tested the resulting phenotypes at 2dpf (Fig. 4B-I).

Our results indicate that F-actin polymerization is essential for normal skeletal growth and inhibition of ectopic branching, while actomyosin contractility plays a minor role in these processes (Fig. 4). The majority of the embryos where MyoII activation was inhibited show minor ectopic branching mostly at the tips of the rods, and some embryos show a delay in skeletal growth (Fig. 4C, D, I). The majority of the embryos where F-actin formation was inhibited show significant reduction of skeletal growth and severe ectopic skeletal branching (similar phenotypes to Fig. 4E, statistics in Fig. 4I). Some embryos show completely arrested skeletal growth (Fig. 4G, I) and in some embryos, additional spicules form (Fig. 4H, I). The co-inhibition of F-actin polymerization and MyoII activity results in skeletogenic phenotypes that resemble those of the inhibition of F-actin alone (Fig. 4I). The phenotypes of Latrunculin-A were more pronounced when the inhibitor was added before spicule formation compared to the addition after the spicules were formed, while the effect of blebbistatin was independent on the time of addition (Fig. 4I). These results indicate that F-actin polymerization is essential for normal skeletal growth and inhibition of ectopic branching throughout skeletogenesis, while MyoII has a minor role in the late stage of these processes.

Strong reduction of skeletal growth and enhanced ectopic branching are common phenotypes to ROCK inhibition and to F-actin inhibition (Figs. 2K-N, P, compared to 4E-G, I). Yet, ROCK inhibition before spicule formation completely blocks skeletogenesis in the majority of the treated embryos (Fig. 2J, P), which was never observed in actomyosin perturbations (Fig 4). Additionally, the formation of an additional spicule observed under F-actin inhibition (Fig. 4H, I), was never observed under ROCK inhibition (Fig. 2). These observations suggest that ROCK's effect on skeletal growth and branching could be through its regulation of F-actin stabilization, but its role in spicule initiation is possibly mediated through its other targets.

ROCK activity is required for F-actin organization around the forming spicule

Next, we tested whether ROCK regulates the actomyosin structure and activity during sea urchin skeletogenesis. To accomplish this we used phalloidin, a fluorophore that binds F-actin specifically, an antibody that detects phosphorylated MyoII (MyoIIP, [46]) and the skeletogenic marker, 6a9 (Fig. 5). In control embryos, F-actin is detected around the tri-radiate calcite spicules at 27hpf (green arrow in Fig. 5B, in agreement with [46, 47]). The pseudopodia cable that connects the skeletogenic cells shows lower F-actin signal compared to the signal around the spicule, possibly since F-actin accumulates around the inner membrane of the spicule, facing the mineral (blue line in Fig. 5B, C, E blue arrows in Fig. 5I, J, L). MyoIIP signal is not enriched in the skeletogenic cells nor in the spicule (Fig. 5D, K). Under continuous ROCK inhibition, the pseudopodia that connects the skeletogenic cells still forms (Fig. 5T) and F-actin accumulation is still observed in the lateral skeletogenic cell clusters; but unlike control embryos, F-actin is not organized and the spicule cavity is not formed (Fig. 5N). MyoIIP signal seems unchanged by ROCK inhibition (Fig. 5P, U), in agreement with the weak and late phenotype of MyoII inhibition (Fig. 4). These findings suggest that ROCK activity is essential for F-actin organization around the spicules, but not for the formation of the pseudopodia cable.

F-actin is enriched at the tips of the spicules independently of ROCK activity

To assess the role of ROCK in actomyosin organization during skeletal elongation we compared F-actin and myoIIP signals between control embryos and embryos where ROCK inhibitor was added at 25hpf (Fig. 6). At the prism stage, F-actin is enriched at the tips of the spicules in both control and ROCK inhibited embryos (white arrowheads in Figs. 6B-E, F-J). We quantified the F-actin signal at the tips compared to the back in both treatments (Fig. 6K, L, see methods for details). The phalloidin signal is on average 3-fold stronger at the tips of the spicules compared to the back, in both control and ROCK inhibition, indicating that F-actin enrichment at the tips is significant and independent of ROCK activity. In both control and ROCK inhibited embryos, the F-actin signal was markedly higher in the regions of the pseudopodia cable where the spicule cavity had formed, compared to the regions where the spicule cavity had not yet formed (blue arrows in Fig. 6B-E, G-J). This again, suggests that F-actin accumulates at the inner membrane of the

spicule cavity that surrounds the mineral. We did not detect an enhanced signal of MyoIIP around the spicules or in the skeletogenic cells, in either condition (Fig. 8D, I). Together these data demonstrate that F-actin coats the spicule cavity, probably in the inner membrane facing the mineral, and is enriched at the tip of the rods, independently of ROCK activity.

At the pluteus stage, F-actin is enriched at the tips of the spicules in both control and ROCK inhibited embryos (white arrowheads in Fig. 6N-Q, S). Some non-skeletogenic cells that are enriched with MyoIIP signal are detected at this time (red arrowheads in O-R). Thus, F-actin enrichment at the tips of the rods correlates with calcium deposition there, but this enrichment does not depend on ROCK activity.

ROCK activity is essential for normal skeletogenic gene expression

The role of ROCK in regulating gene expression during vertebrates' chondrocytes, osteoblasts and odontoblasts differentiation [20, 34, 35] intrigued us to study the role of ROCK in regulating skeletogenic gene expression in the sea urchin embryo. ROCK continuous inhibition significantly downregulates the expression of multiple skeletogenic genes, including the cytoskeleton remodeling gene, *rhogap24l/2*, the biomineralization genes, *caral7, scl26a5* and *SM30* at 27hpf and 2dpf (Fig. 7A, [6]). ROCK inhibition did not affect the expression level of VEGFR and ROCK itself at these times (Fig. 7A). Washing the inhibitor after 25hpf or adding the inhibitor at 25hpf had a weaker effect, but still lead to downregulation of *caral7*, *SM30*, *angio1* and *notch1* (Fig. 7B). Thus, ROCK activity is required for the activation of multiple skeletogenic genes during sea urchin skeletogenesis.

Both continuous and late ROCK inhibition, strongly affects the spatial expression of key regulatory and biomineralization genes that are normally expressed differentially within the skeletogenic lineage at the pluteus stage (Fig. 7D-L). These include, the skeletogenic transcription factors, Ets1, Alx1 and Erg1 that are essential for skeletogenic cell specification and biomineralization [36, 65], the transcription factors Hex and MyoD1, VEGF receptor (VEGFR) and the biomineralization genes *SM50* and *SM30*. In normal plutei these genes are differentially expressed within skeletogenic lineage, but in both continuous and late ROCK inhibition the expression of these genes becomes localized to

the two lateral skeletogenic cell clusters and their vicinity (Fig. 7D-L). The lateral skeletogenic cells clusters are the cells where these genes are expressed in the gastrula stage (24-27hpf) and where spicule formation begins in normal embryos [6, 44]. The expression of VEGFR and SM50 under ROCK inhibition is more expanded than the other tested genes and is also observed at the tips of the anterolateral rods (Fig. 7I, K). The VEGF ligand that is normally expressed in the ectodermal cells near the four tips of the post-oral and anterolateral rods [44], is expressed at four ectodermal domains near the lateral skeletogenic cell clusters and near the end of the anterolateral chain, under ROCK inhibition (Fig. 7J).

Overall, under ROCK inhibition, the expression of key regulatory and biomineralization genes is downregulated (Fig. 7A) and remains localized to the area near the lateral skeletogenic cells clusters (Fig. 7D-I, K, L). This localization is despite the proper formation of the dorsal, anterolateral and mid-ventral chains (Fig. 7C). This implies that ROCK activity and possibly, skeletal elongation itself, provide regulatory cues to the skeletogenic GRN required for the dynamic progression of gene expression within the skeletogenic lineage.

Discussion

Biomineralization is a complex molecular process, encoded in the species genome and executed by the GRNs and the cellular machinery. Here we used the sea urchin larval skeletogenesis to investigate the role of ROCK and the actomyosin network in biomineral formation and in regulating gene expression, as we summarize in Fig. 8. ROCK expression is enriched in the skeletogenic cells, partially depending on VEGF signaling (Figs. 1, S2). ROCK activity is necessary for spicule formation, skeletal elongation and prevention of ectopic skeletal branching (Figs. 2, 3, S4). Direct inhibition of F-actin polymerization results in similar but not identical skeletogenic phenotypes (Fig. 4) and F-actin is organized around the spicule cavity and enriched at the spicule tips (Figs. 5, 6). ROCK activity feeds back into the skeletogenic GRN and affects regulatory and biomineralization gene expression (Fig. 7). Below we discuss our findings and their implications for the biological control and evolution of biomineralization.

The first step in generating the sea urchin spicules is the construction of the spicule cavity, a membrane filled with calcium carbonate and coated with F-actin (Fig. 8A). ROCK activity is necessary for the formation of the spicule cavity and for the organization of F-actin around it (Figs. 2, 5, 8B). A direct perturbation of F-actin polymerization strongly disrupts spicule growth and shape (Fig. 4). F-actin is enriched in the regions of the pseudopodia cable that are filled with mineral, supporting its localization to the inner membrane of the spicule cavity (Figs. 5, 6, Fig. 8A). F-actin accumulation in the inner membranes of the spicule cavity could be providing cues and structural support for the exocytosis of mineral-bearing vesicles into the cavity, as we explain below (Fig. 2H, [26-28, 66]). Overall, our studies indicate that ROCK activity is essential for the formation of the spicule cavity and for the initial F-actin organization around it, which could be essential for mineral deposition into it (Fig. 8C).

After the spicule cavity has formed, the spicules elongate inside the pseudopodia chord by mineral deposition at the tips of the spicule rods, which depends on ROCK activity and on F-actin polymerization (Figs. 2-4, 8E, F). F-actin is detected along the spicules and is significantly enriched at the tips of the elongating spicules, likely around the inner membrane of the spicule cavity (Fig. 8D, [26]). F-actin enrichment at the tips is independent on ROCK activity (Fig. 6A-M, 8E, F), yet under ROCK inhibition and under the inhibition of F-actin polymerization, ectopic branching is observed at the tips and in the back (tip splitting and spicule dripping, Figs. 2P, 3A, 4I). The participation of F-actin and ROCK in polarized tip-growth and vesicle exocytosis has been observed in both animals and plants [26, 67]. F-actin is used for short range myosin trafficking of vesicles toward the secretion site [26, 66]. Once the secretory vesicle fuses with the membrane, it is coated with F-actin that stabilizes the vesicle and enables MyoII binding and ROCK-regulated contraction, necessary for the content secretion [27, 28]. In plant cells, F-actin accumulate at the growing tip of the cell and assists vesicle exocytosis necessary for polarized tip-growth [67]. Our observations suggest that ROCK and F-actin could be regulating the localized exocytosis of mineral-bearing vesicles during sea urchin skeletogenesis. The delay in spicule growth and the ectopic branching could be due to impaired and misplaced vesicle trafficking and deposition under ROCK and F-actin inhibition, but the exact protein regulatory network is still to be determined.

ROCK activity is necessary for correct spatiotemporal expression of regulatory and biomineralization genes (Fig. 7, 8D-F). ROCK inhibition downregulates the expression level of skeletogenic genes (Fig. 7A) and prevents the spatial progression of key skeletogenic genes toward the edges of the skeletal rods (Fig. 8E). In other systems, ROCK activity was shown to regulate gene expression through various intracellular pathways including YAP, SRF and extracellular signal-regulated kinase (Erk) [68-70]. Furthermore, ROCK has an important role in mechano-sensing of matrix rigidity and transducing it into changes in gene expression [71]. Relatedly, stiff matrix activates ROCK in pre-osteoblastic cells, which activates Erk that leads to osteogenic differentiation and upregulation of osteogenic gene expression [70]. Sea urchin ROCK could be sensing the spicule stiffness and transducing it into gene expression, providing a necessary feedback between spicule elongation and the skeletogenic GRN. Further studies are required to identify the specific molecular mechanisms activated by ROCK to affect gene expression in the skeletogenic cells.

Our findings and the role of actomyosin remodeling in biomineralization, from calcifying and silicifying single cells to vertebrates bones and teeth, suggest that this molecular machinery is a part of the common molecular tool-kit of biomineralization: There is a tight association between actin filaments and the biomineralization compartment in diatoms [33] and a highly dynamic actin organization that forms the biomineralization compartment in foraminifera [31]; Perturbations of actin polymerization result with severely deformed shells and inhibition of shell shedding in coccolithophores [29, 30] and diatoms [32]; In vertebrates' biomineralizing cells, chondrocytes, osteoblasts, osteocytes and odontoblasts, actomyosin remodeling and ROCK participate in cell differentiation and mechano-transduction [20, 34, 35, 70]. Most likely, the actomyosin network was employed independently, downstream of convergent GRNs across Eukaryotes, to control vesicular motion and secretion and to generate the biomineralization compartment.

Methods

Animal and embryos

Adult *Paracentrotous lividus* were obtained from the Institute of Oceanographic and Limnological Research (IOLR) in Eilat, Israel. The animals were kept in aquaria in a

dedicated room, in artificial seawater (ASW) with the salinity of 39 ppt. Eggs and sperm were obtained by injection of 0.5M KCl solution into the adult sea urchin species. Embryos were cultured at 18°C in 0.2µ filtered ASW.

Imaging

Embryonic phenotypes and WMISH were imaged by Zeiss Axioimager 2. Fluorescent markers were imaged using Nikon A1-R Confocal microscope. All images were aligned in Adobe photoshop and Illustrator. Statistical analysis and graphs were done using Excel (version 16.53) and SPSS (version 25).

Axitinib (AG013736) treatment

5mM stock solution of Axitinib (AG013736, Selleckchem, Houston, TX, USA), was prepared by reconstituting the chemical in dimethylsulfoxyde (DMSO). The embryos were treated with Axitinib at a final concentration of 150nM. Control embryos were cultured in similar concentrations of DMSO at no more than 0.1% (v/v).

Western Blot

Embryo cultures treated with 150 nM Axitinib, or DMSO as control, were collected at 22hpf, 27hpf and 33hpf by centrifugation of 10,000g for 2 minutes. We lysed the pellet in 150µL lysis buffer (20 mM Tris-HCl, 150 mM NaCl, 1% Triton X-100, pH 8) with protease inhibitors (protease inhibitor cocktail w/o metal chelator; Sigma, P8340; 1:100) and phosphatase inhibitors (50 mM NaF, 1 mM Na3VO4, 1 mM Na4P2O7, 1mM, βGP) as described in [72]. 40µg protein were loaded on 8% SDS-acrylamide gel, transferred to PVDF membranes for Western blot analysis. Anti-ROCK antibody (ab45171, Abcam) was used in a 1:300 dilution followed by anti-rabbit HRP secondary antibody diluted to 1:2500 (Jackson ImmunoResearch 111-035-003). For the loading control, the membrane was incubated with anti-β-tubulin antibody (1:5000; Sigma) followed by anti-mouse antibody 1:5000 (Jackson ImmunoResearch 115-035-003). Quantification of ROCK signal was done using Image studio lite vr. 5.2. ROCK signal was divided by Tubulin signal and then the ratio between ROCK/Tubulin in control vs. VEGFR inhibition was calculated. The graph in Fig. S2 was generated based on three biological replicates (different sets of parents).

Immunostaining procedure

Phalloidin labeling, MyoIIP (p20-MyosinII), ROCK (anti ROCK2+ROCK1 antibody [EP786Y], AB-ab45171, Abcam), and 6a9 immunostaining were done similarly to (36, 37) with minor modifications. Embryos were fixed in 4% paraformaldehyde (in 33mM Maleic acid pH7 and 166mM NaCl) for 30 minutes at room temperature. Then washed four times with PBST. Embryos were incubated for one hour in PBST-blocking solution (PBST with 4% sheep serum), followed by incubation with primary antibody against MyoIIP (Anti-Myosin light chain (phospho S20) Abcam- ab2480, Rabbit, 1:200 dilution), together with 6a9 antibody (mouse 1:3 dilution) in blocking solution overnight, at 4°C. Embryos were then washed four times in PBST, then treated with secondary Antibodies (Cy3-Goat Anti Rabbit IgG 1:200, 111-165-144 Jackson ImmunoResearch, and 405-Goat anti Mouse IgG 1:100, 14981, respectively) in PBST-blocking solution and incubated for 40 minutes in room temperature. This was followed by 3 PSBT washes, 2 PBSx1 washes, incubation with 50mM ammonium chloride in PBS for 5 min, 3 washes in PBS, incubating with blocking solution (PBS with 4% serum) for 10 minutes in room temperature. Embryos were then treated with hyaluronidase [750 U/ml in PBS (Sigma H3506)] for 10 min, followed by two washes in PBS and one hour in PBS-blocking solution. Overnight phalloidin 1:500 (PHDG1, Cytoskeleton Inc) in Blocking solution. Embryos were washed three times in PBS, incubated in PBS-blocking solution for 20 minutes and washed again in PBS and observed under confocal microscope.

Quantification of Anti-ROCK and Phalloidin signal

A graphical program was written to allow manual quantification of the fluorescent signal from the spicule regions by identifying “stained” pixels per selected area. For ROCK immunostaining, embryos at 22hpf, 27hpf and 33hpf in control and under VEGFR inhibition were used, and regions in the skeletogenic cells or in the ectoderm were selected. A global threshold was chosen to identify the “stained” pixels. The ratio of stained anti-ROCK to region total area was compared between ectodermal and skeletogenic cells, and between control and VEGFR inhibited embryos. For phalloidin analyses, embryos at 33hpf of control and ROCK inhibitor addition at 25hpf were used and for each image, two regions were selected: an area at the tip of the spicule and an area at the back of the spicule, about

~10 microns apart. The ratio of stained phalloidin to region total area was compared between tip and back, in control and ROCK inhibited embryos. Paired t-test was used to compare the differences in phalloidin signal between the tip and back of the spicules across all groups. t-test was used to compare tip/back ratio of Phalloidin signal between control and ROCK inhibited embryos.

ROCK MASOs injections

Microinjections were conducted similarly to [44]. The eggs were injected with an injection solution containing 0.12M KCl, 0.5µg/µl Rhodamine Dextran and 900µM of MASOs. Downregulation of *ROCK* was done by injecting two specific MASOs targeting the translation sites of the pre-mRNA. MOSOs were designed and synthesised by Gene Tools, Philomath, OR, according to ROCK sequence. The sequence of ROCK MASO-1 (5'-AGACATATTTGGAGCCGACATCCTG-3') matches the start of translation region (ATG, marked in green), and ROCK MASO-2 (5'-TCTCTTGCGTTATATTCCACTAAGT-3') that matches the 5' region upstream of the start of translation. Control embryos were injected in the same concentration with Random MASO. Injected embryos were cultured at 18°C, imaged and scored at 2dpf.

ROCK inhibitor (Y27632) treatment

Y27632 is a specific inhibitor to the ATP site of ROCK's kinase domain and competitively inhibits the phosphorylation of its targets (28). Y27632 stock (10005583 CAS Regisrty No. 129830-38-2, Cayman chemical), was prepared by reconstituting the chemical in dimethylsulfoxyde (DMSO). The embryos were treated with Y27632 at a final concentration between 30-80µM, as mentioned in the results. When we wanted to investigate the branching pattern in the inhibitor-addition experiments we used 30-40µM, which leads to large spicules with prominent ectopic branching (Fig. 2P). In the continuous experiments we mostly used 80µM, which gives a robust phenotype of either spicule loss or spicule initiations (Fig. 2P). Throughout the paper, control embryos were cultured in DMSO at the same volume as Y27632 solution and no more than 0.1% (v/v).

Spicule preparation for micro-computed tomography (SR-µCT) measurement

Control embryos and embryos where 40µM Y27632 was added at 25hpf, were collected by centrifugation of 50mL Falcon tubes at 2000rpm, at 48h and 72hpf. Every tube was washed in 10 mL cold distilled water (DW), transferred into epi-tube and washed three times in 1mL cold DW (incubation at 4˚C between every wash, centrifuge at 2000rpm in room temperature for 2min). Then the skeletons were washed three times in 3% NaOCl followed by three washes in DW, one wash in 70% EtOH and one wash in Acetone. Skeletal spicules were dried at room temperature and stored at -20 ˚C.

Synchrotron and lab-based SR-µCT

Dry and loose skeletal spicules prepared as described above, were used for the SR-µCT analysis. We analyzed 14 sets of spicules from three (control) and four (ROCK inhibited) pairs of parents, divided into four groups: 2dpf, control, n=44; 2dpf ROCK inhibited, n=93; 3dpf control, n=51; 3dpf ROCK inhibited, n=93, see Table S1). Spicules were glued to sharpened toothpick tips, either in bulk ('rinsing' spicules over the liquid glue) or individually when picked by hand by means of a brush bristle. Each toothpick loaded with spicules, was mounted on a 3ml vial twist-off lid and for transportation securely stored in the vial (Fig. S5A, B). Typically, hundreds to a dozen spicules were attached to tooth picks in bulk and individual preparations, respectively. For each set 2-3 µCT-samples were prepared, which allowed the acquisition of statistically relevant sample sizes (40+ spicules/group, Table S1). Tomographic data sets were acquired using the following scanning parameters; for the lab based µCT (RX Solutions, Chavanod, France) 90kV, 143-160µA, 1440 images, average frames 10, frame rates 0.4-1, voxel sizes: 0.45-59µm; and for the synchrotron radiation µCT (Anatomix, Synchrotron SOLEIL, Gif-sur-Yvette, France) 2048 images, angle between projections 0.09°, voxel size: 0.65µm. Tomographic data reconstruction was performed with commercial (RX Solutions, Chavanod, France) and custom-built software (Anatomix, Synchrotron SOLEIL, Gif-sur-Yvette, France) at the MPICI and at Anatomix, SOLEIL, respectively.

Three-dimensional (3D) data analysis

Data visualization, pre-processing including cropping and image type conversion to 16bit (of the Sr- µCT data), and user-augmented segmentation of intact spicules were performed

in Amira using off-the-shelf modules (Fig. S5C-E, [73]). The grey level segmentation of the spicules was mostly done with the same threshold value on the greyscale across all data sets. Volume and area measurements were performed on the segmented spicules, *i.e.* the label-fields using Amira's material.statistics module (Volume3D and Area3D). Average spicule thickness and total length measurements were performed with python code, utilizing available python libraries (*e.g.*, skimage, skan, scipy). The code was applied to 3D-tif files created from Amira's label-fields, which contained the segmented spicules. For length measurements, the spicules were skeletonized and the chord lengths of the branches forming a spicule-skeleton were summed up to obtain the total spicule length. For thickness measurements, we performed Euclidean distance transforms for each spicule using scipy's ndimage.morphology.distance_transform_edt package, and calculated the average spicule thickness based on the distance measurements obtained at each voxel from spicule-skeleton to the nearest spicule surface. Quality control of our measurements was performed with open source software, Fiji and available plugins (e.g. BoneJ, FiberJ, DiameterJ).

Calcein staining

A 2mg/ml stock solution of blue calcein (M1255, Sigma) and a 2mg/ml stock solution of green calcein (C0875, Sigma) were prepared by dissolving the chemicals in distilled water. Working solution of 250µg/ml and 150µg/ml, respectively, was prepared by diluting the stock solution in artificial sea water. Blue calcein was added to the embryo culture at 29hpf for one hour and then washed. At 44hpf the green calcein was added for one hour and washed. For FM4-64 staining A 100µg/ml stock solution of FM4-64 (T13320, Life technologies, OR, USA) was prepared by dissolving the chemical in distilled water. Working solution of 2.5 µg/ml was prepared by diluting the stock solution in artificial sea water. Embryos were immersed in working solution about 10 minutes before visualization.

Latrunculin-A and Blebbistatin treatments

Latrunculin-A (Lat-A) is used to depolymerize actin by binding the actin monomers and prevent them from polymerization (34). 1mM of Lat-A stock (L12370, Thermo Fisher Scientific) was prepared by reconstituting the chemical in DMSO. The embryos were treated with Lat-A at final concentration of 2 µM.

Blebbistatin (Blebb) inhibits non-muscle myosin II, its inhibitory effect is by binding to the ATPase intermediate with ADP and phosphate bound at the active site, interfering with the phosphate release (35). 1mM of Blebb stock (13013-5, Enco) was prepared by reconstituting the chemical in DMSO. The embryos were treated with Blebb at final concentration of 2 µM. For the double inhibition experiments, embryos were treated with Blebb at final concentration of 1.5 µM, and with Lat-A at final concentration of 2 µM.

WMISH procedure

WMISH was performed as described in [42, 44]. List of the primers used to make the WMISH probes is available in [44].

cDNA preparation for QPCR experiments

For ROCK inhibition experiments total RNA was extracted from >1000 sea urchin embryos in each condition using RNeasy Mini Kit (50) from QIAGEN (#74104) according to the kits' protocol. DNase treatment on column was done using RNase-Free DNase Set-Qiagen (50) (#79254). RNA was reverse-transcribed using the High Capacity cDNA RT kit, AB-4368814 (Applied Biosystems) following the manufacturer's instructions.

Quantitative polymerase chain reaction (QPCR)

QPCR was carried out as described in [44]. Complete list of primer sequences used for the experiments in provided there.

Acknowledgments

We are grateful to SOLEIL for provision of synchrotron radiation facilities and we would like to thank Dr. Mario Scheel, Dr. Timm Weitkamp and Dr. Jonathan Perrin for assistance in using beamline ANATOMIX for nano and µCT. We thank the Bioimaging Unit, Faculty of Natural Sciences, University of Haifa for assistance with the use of confocal. We thank Charles Ettensohn for the generous gift of the 6a9 antibody produced in his lab. We thank David Ben-Ezra and Michael Kantorovitz for their help with sea urchin handling. We thank Haguy Wolfenson for illuminating discussions of the results and conceptual framework. We thank Alvaro Israel and Omri Nahor for their help with sea urchin maintenance. We thank Yulia Kagan for her help with the western blot.

Funding: Israel Science Foundation grant number 211/20 (S.B.D.), and Zuckerman fellowship (M.R.W.), TUD internal funding (YP).

Author contributions:

Conceptualization: EH, TG, ML, SBD
Methodology: EH, TG, RS, MW, LB, ML, YP
Investigation: EH, TG, RS
Visualization: EH, RS, SBD
Supervision: TG, SBD, LB, YP
Writing—original draft: EH, SBD
Writing—review & editing: EH, TG, RS, MW, ML, YP, SBD

Competing interests: Authors declare that they have no competing interests.

Data and materials availability: All data are available in the main text or the supplementary materials.

Figures

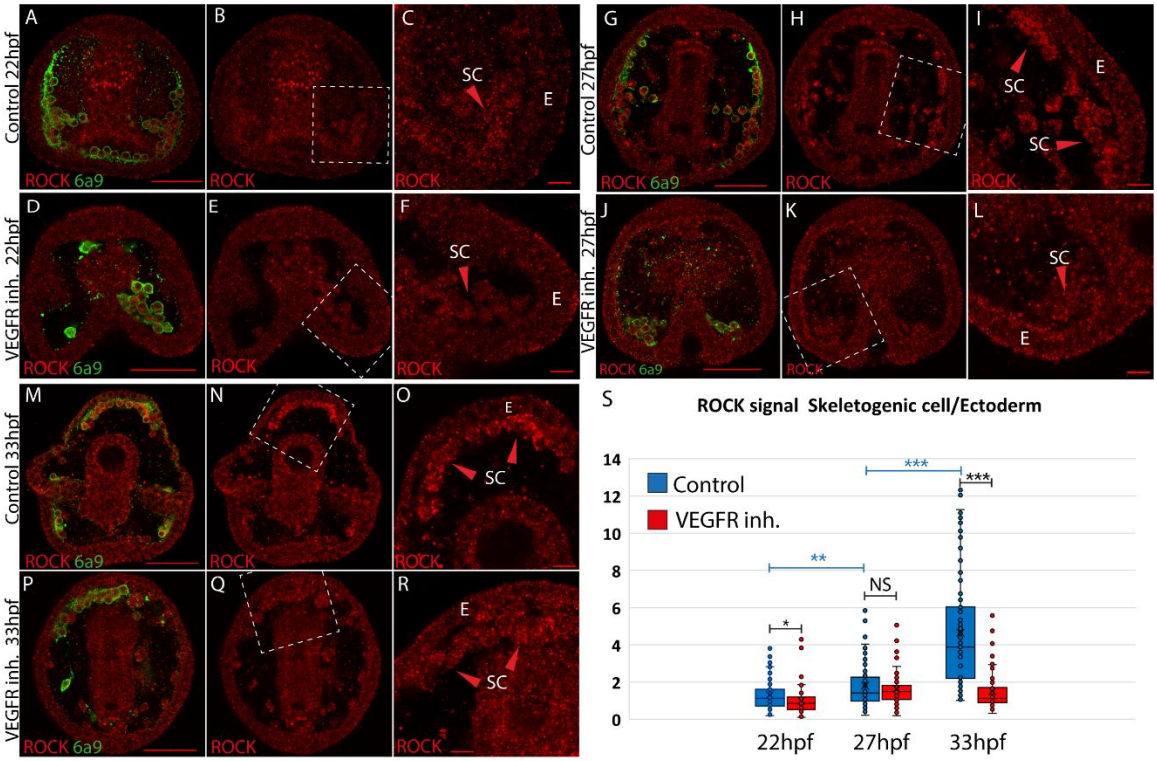

Figure 1 ROCK enrichment in the skeletogenic cells increases with time and depends on VEGF signaling. A-R, ROCK immunostaining at different times points in control and under VEGFR inhibition. In each condition and time point, the left image shows ROCK immunostaining and the skeletogenic cell marker, 6a9 (A, D, G, J, M and P). The middle image shows ROCK immunostaining alone in the whole embryo (B, E, H, K, N and Q). The right image shows the enlargement of the white rectangle region of the middle image (C, F, I, L, O, R). Scale bar in whole embryo is 50µm and in enlargements is 10µm. E – ectoderm, SC – skeletogenic cells. S, quantification of the ratio between ROCK signal/area in the skeletogenic cells compared to the ectodermal cells (see methods for details). Each box plot shows the average marked in x, the median, the first and the third quartiles (edges of boxes) and all experimental measurement (dots). Experiments were performed in three independent biological replicates and in each condition at least 33 embryos were measured. Statistical significance was measured using paired 2-tailed t-test where, * indicates $P<0.05$, ** indicates $P<0.005$, and *** indicates $P<0.0005$. The average ratios and ztest for significance difference from 1, are 22hpf control ~1.3, z=0.0006; VEGFR inhibition ~1, z=0.5, 27hpf control ~1.8, $z<10^{-11}$; VEGFR inhibition ~1.6, $z<10^{-8}$, 33hpf control ~4.6, $z<10^{-23}$; VEGFR inhibition ~1.5, $z<10^{-5}$.

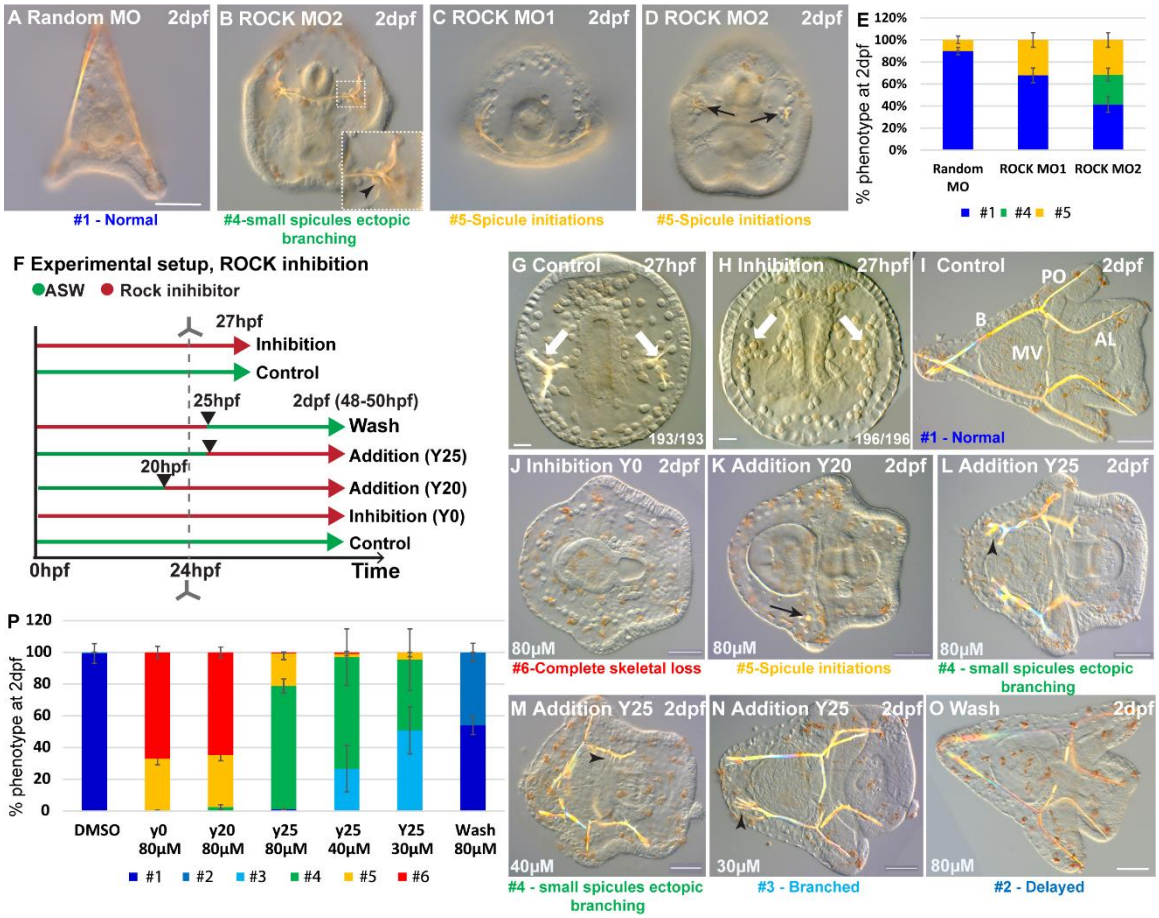

Figure 2 ROCK activity is essential for spicule formation and for normal elongation and branching morphology. A-E, genetic perturbation of ROCK translation using two different MASOs observed at 2dpf. A, control embryo injected with Random MASO develops normal skeleton. B, embryo injected with ROCK MO-2 shows ectopic spicule branching. C, D, embryos injected with ROCK MO-1 or MO-2 show spicule initiations. E, summary of MASO injection phenotypes based on 4-6 independent biological replicates, exact numbers are provided in Table S1. F-O, Pharmacological perturbations of ROCK activity using the inhibitor Y27632. F, experimental design of the various ROCK treatments showing the time of inhibitor addition/wash. G, Representative control embryo and H, embryo under ROCK inhibition using 80µM Y27632 at 27hpf. Results are based on four biological replicates and number of scored embryos that show the reported phenotype out of all embryos scored is indicated at the bottom of G and H. I-O, various skeletogenic phenotypes due to ROCK inhibition at different times and concentrations, observed at 2dpf. Treatment and concentrations are indicated for each image. I, the skeletal rods in control embryo are B, body; AL, anterolateral; PO, post-oral and MV, midventral. P, summary of ROCK perturbation phenotypes at 2dpf. Color codes of phenotypes match the color of the phenotypes reported in I-O. Results are based on 3-8 biological replicates for the different treatments, exact number of replicates and embryo scores for each experiment is provided in Table S1.

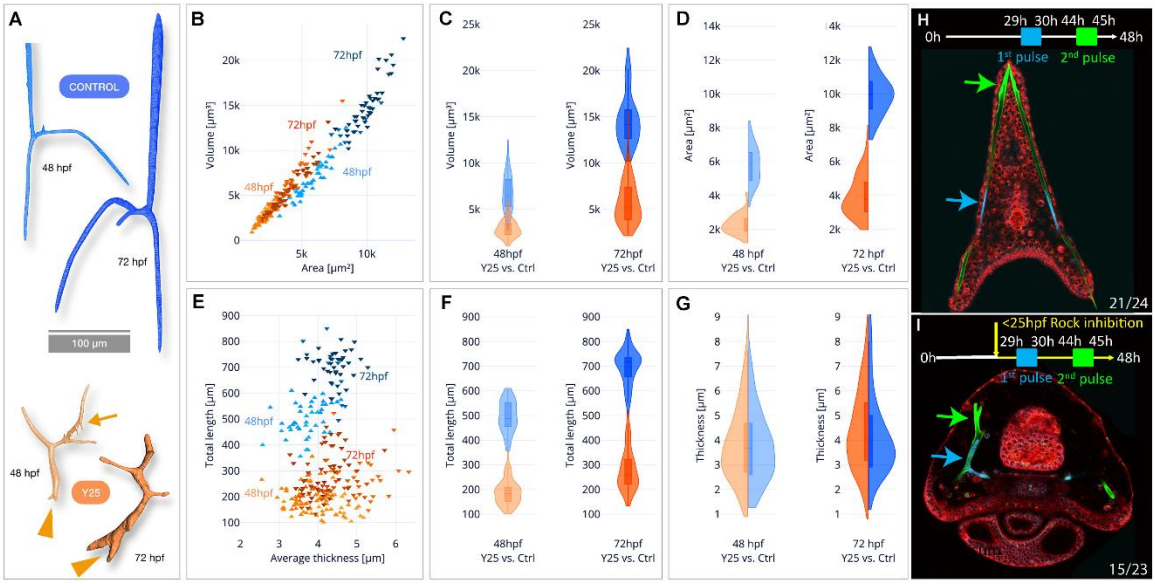

Figure 3 SR-µCT studies of ROCK inhibited spicuels show reduction in skeletal volume, surface area and total length, but not thickness and 2-pulse calcein shows loss of tip-dominance. A, Exemplary 3D-renderings of control spicules (top, blue) and spicules where 40µM of ROCK inhibitor was added at 25hpf (bottom, orange), dissected at 48hpf and 72hpf. Arrowheads point to tip splitting and arrow at 48hpf point to spicule dripping at the back. B, Spicule volume vs. area for control and ROCK-inhibited spicules at 48 and 72 hpf. Each data point represents a single spicule. C-D, Frequency distributions for volume and surface area of control and ROCK-inhibited spicules at 48 hpf and 72 hpf (left and right violin plots, respectively). E, Spicules' total branch length and average thickness for control and ROCK-inhibited spicules at 48 and 72 hpf. F-G, Frequency distributions for spicule lengths and thickness of control and ROCK-inhibited spicules dissected at 48hpf and 72hpf (left and right violin plots, respectively). H, I, Calcein two-pulses experiment shows loss of tip-dominance under ROCK inhibition. Embryos were exposed to blue calcein from 29-30hpf, and to green calcein from 44-45hpf. Embryos were stained with FM4-64 membrane marker (red) prior to image acquisition at 48hpf. H, Control embryo, G, Embryo where 30µM of Y27632 was added at 25hpf. The experiments were done in three biological replicates and the numbers at the bottom indicate the number of embryos that show this phenotype out of all embryos scored.

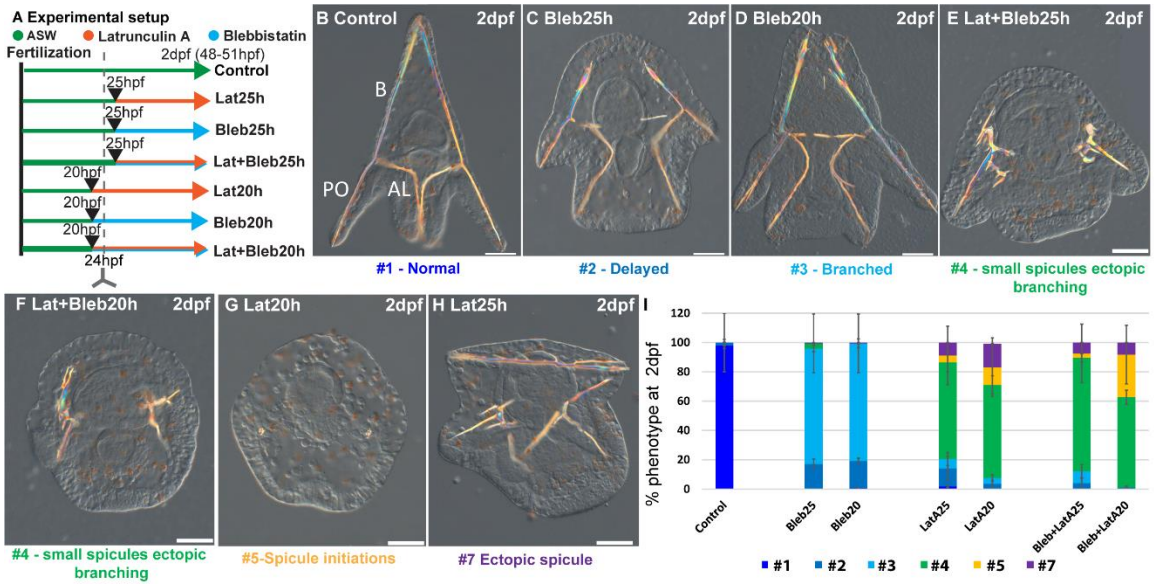

Figure 4 Perturbations of actin polymerization and myosin activation reduce skeletal growth and increase branching. A, experimental design of the various Latrunculin-A and Blebbistatin treatments showing the time of inhibitor addition. B-H, representative embryos showing the effect of actomyosin perturbations. B, control embryo showing the skeletal rods where B - body, PO – postoral, AL – anterolateral rods. C, D, embryos treated with 2μM Blebbistatin after 25hpf (C) and after 20hpf (D). E, F embryos treated with 2μM Latrunculin-A and 1.5μM Blebbistatin after 25hpf (E) and after 20hpf (F). G, H, embryos treated with 2μM Latrunculin-A after 20hpf (G) and after 25hpf (H). I, Statistics of Latrunculin-A and Blebbistatin phenotypes, color code of phenotype is indicated in the representative images. Error bars indicate standard deviation. All treatments were conducted in at least three biological replicates and exact number of replicates and scored embryos are provided in table S4. Scale bar is 50μm.

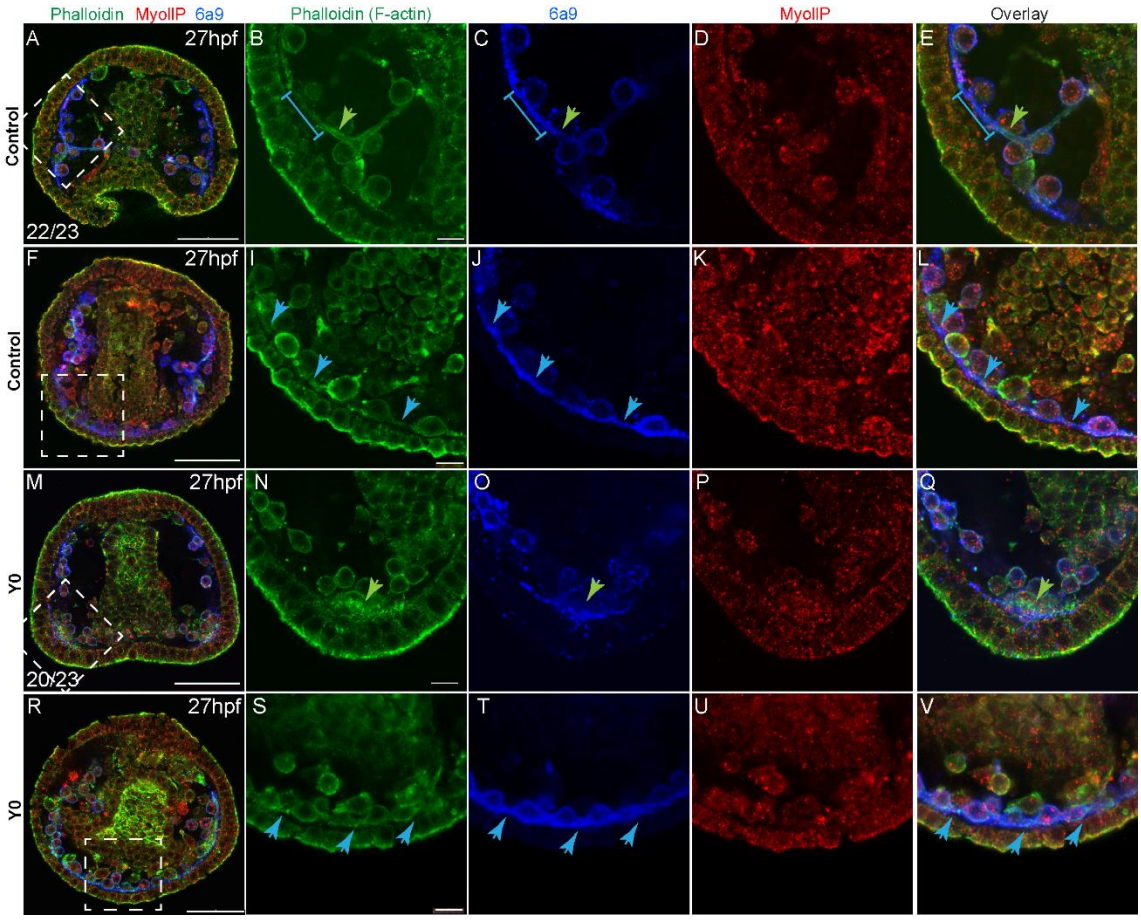

Figure 5 ROCK inhibition interferes with F-actin organization around the spicule but the pseudopodia cable between the skeletogenic cells still forms. Representative images showing normal embryo (A-L) and embryos treated with ROCK inhibitor from fertilization (M-V, 80μM), at 27hpf. Phalloidin (green) was used to stain F-actin, MyollP (red) was used to stain phosphorylated myosinII and 6a9 (blue) was used to mark the skeletogenic cells. Right panels show enlargements of the rectangle sections marked in the left most panels. Green arrows point to regions that show enriched F-actin signal, blue arrows point to the pseudopodia cable. The blue line in B, C and E marks a region of the pseudopodia cable that is stained by 6a9 but has low F-actin signal. The experiments were done in 3 biological replicates, the numbers at the bottom left of (A, M) indicate the number of embryos that show this phenotype out of all embryos scored. Scale bar in A, F, M and R is 50μm, and in B, I, N and S is 10μm.

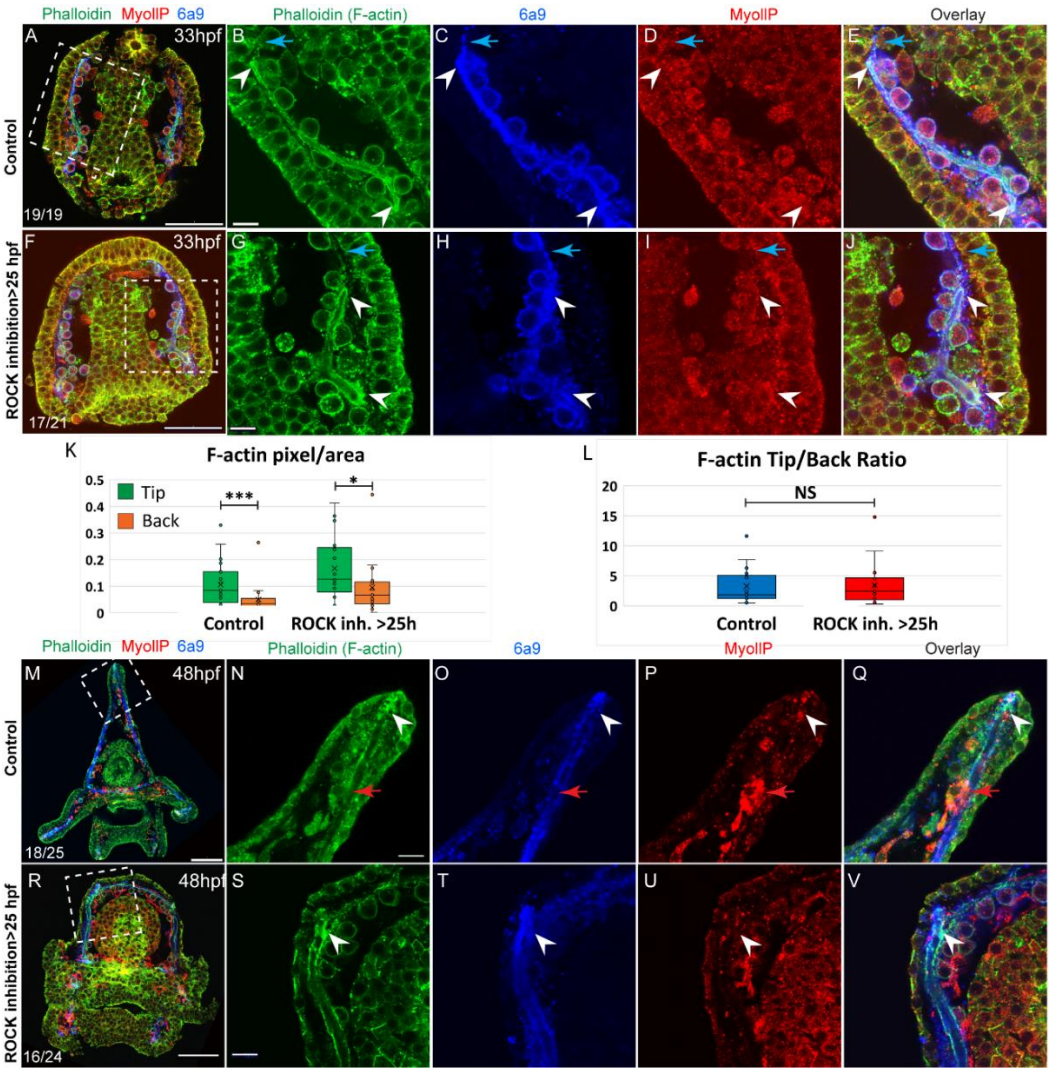

Figure 6 During skeletal elongation F-actin filaments are enriched at the tips of the rods independently on ROCK Activity. A-J, representative images at 33hpf, showing normal embryo (A-E) and embryos treated with ROCK inhibitor from the gastrula stage (>25hpf, 30µM, F-J). Embryos are stained with Phalloidin (green), MyollP antibody (red) and 6a9 (blue). B-E, G-J, enlargement sections of the spicule area marked with rectangle in A and G. White arrowheads point to the enriched F-actin signal at the tips. Blue arrows point to the region of the pseudopodia cable that is not filled with the spicule cavity. K, L, quantification of the tip to back F-actin signal (number of green pixels per area) at 33hpf in control embryos and ROCK inhibition >25hpf. Each box plot shows the average (x), median (middle line), the first and the third quartiles and all the points measured. Asterisks indicate statistical significance in paired t-test, where * is $p<0.05$ and *** is $p< 0.0005$, NS- not significant. M-V, similar experiments to A-J, at 48hpf, 40µM of ROCK inhibitor added at 25hpf. Red arrows point to non-skeletogenic cells enriched with MyoIIP. The experiments were repeated in 3 biological replicates and the numbers at the bottom left of (A, F, M, R) indicate the number of embryos that show this phenotype out of all embryos scored. Scale bar in A, F, M, R is 50µm and in B, G, N, S, is 10µm.

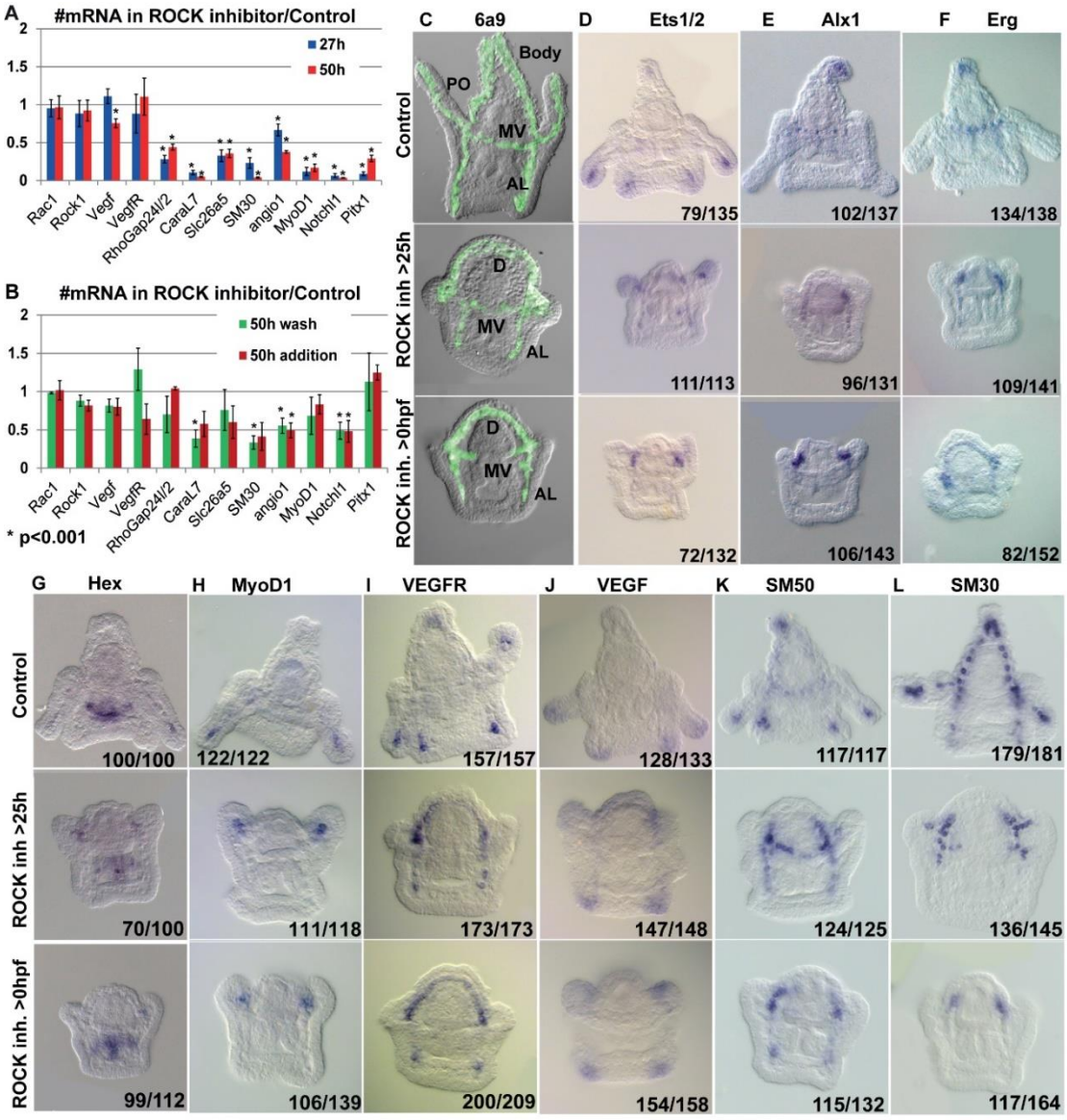

Figure 7 ROCK activity is essential for normal gene expression in the skeletogenic cells. (A) the effect of continuous ROCK inhibition on gene expression levels at 27hpf and 50hpf. (B) the effect of the addition of ROCK inhibitor at 25hpf and the wash at 25hpf of ROCK inhibitor added at 0hpf on gene expression level at 50hpf. Inhibitor concentration is 80µM and the QPCR experiments are based on 4 biological replicates in (A) and 3 in (B) Asterisks indicate $p<0.001$, one tailed z-test. Error bars show standard deviation. (C-L) Representative images of control embryo (top panels), embryos where ROCK inhibitor was added at 25hpf (middle panels), and embryos that were exposed to continuous ROCK inhibition (bottom panels), at the pluteus stage (~48hpf). (C) skeletogenic cell marker, 6a9. MV, midventral; AL, anterolateral, and PO, Post-oral rods, D, dorsal skeletogenic chain. (D-L) spatial expression of skeletogenic genes. Gene names are indicated at the top of each panel. Numbers at the bottom of each image indicate the number of embryos that show this phenotype (left) out of all embryos scored (right), conducted in at least three independent biological replicates.

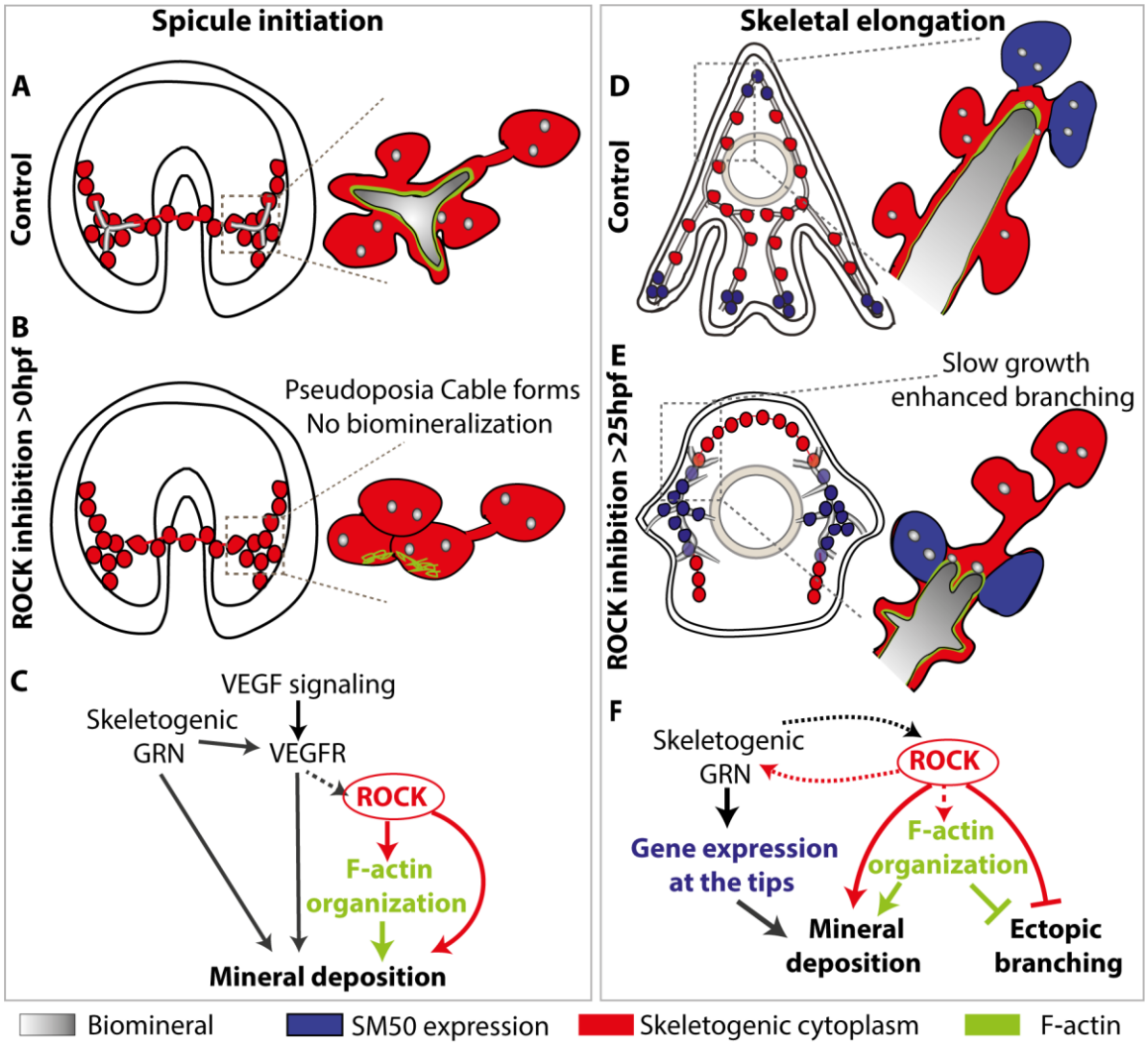

Figure 8 A model of ROCK regulation of spicule formation and elongation. A, B, at the gastrula stage (~27hpf in *P. lividus*), the triradiate spicule is coated with F-actin in normal embryos (A). ROCK continuous inhibition prevents spicule formation. F-actin enrichment is detected in the skeletogenic cells at the lateral clusters but is not organized. C, a model of the regulation and activity of ROCK and F-actin during the first stages of spicule initiation (~24-27hpf in *P. lividus*). VEGF signaling is required for the early skeletogenic cell migration and for the enrichment of ROCK in the skeletogenic cells. ROCK activity is required for spicule initiation and for F-actin organization around the spicules. D, during skeletal elongation F-actin is detected around the spicule cavity and is enriched at the tips of the rods. The expression of SM50 and some other skeletogenic genes, is localized to the tips of the rods. D, under the addition of ROCK inhibitor, skeletal growth rate is reduced and ectopic spicule branching is observed. The expression of skeletogenic genes is localized to the vicinity of the growing rods and does not progress to the edges of the dorsal and anterolateral chains. F, a model of the regulation and activity of ROCK and F-actin during skeletal elongation.

References

1. Evans JS. The Biomineralization Proteome: Protein Complexity for a Complex Bioceramic Assembly Process. Proteomics. 2019;19(16):e1900036. Epub 2019/06/21. doi: 10.1002/pmic.201900036. PubMed PMID: 31219243.
2. Kawasaki K, Buchanan AV, Weiss KM. Biomineralization in humans: making the hard choices in life. Annu Rev Genet. 2009;43:119-42. Epub 2009/08/08. doi: 10.1146/annurev-genet-102108-134242. PubMed PMID: 19659443.
3. Murdock DJE. The 'biomineralization toolkit' and the origin of animal skeletons. Biol Rev Camb Philos Soc. 2020;95(5):1372-92. Epub 2020/05/25. doi: 10.1111/brv.12614. PubMed PMID: 32447836.
4. Weiner S, Addadi I. Crystallization Pathways in Biomineralization. Annu Rev Mater Res. 2011;41:21-40.
5. Ben-Tabou de-Leon S. The Evolution of Biomineralization through the Co-Option of Organic Scaffold Forming Networks. Cells. 2022;11(4). Epub 20220209. doi: 10.3390/cells11040595. PubMed PMID: 35203246; PubMed Central PMCID: PMCPMC8870065.
6. Morgulis M, Gildor T, Roopin M, Sher N, Malik A, Lalzar M, et al. Possible cooption of a VEGF-driven tubulogenesis program for biomineralization in echinoderms. Proc Natl Acad Sci U S A. 2019;116(25):12353-62. Epub 2019/06/04. doi: 10.1073/pnas.1902126116. PubMed PMID: 31152134; PubMed Central PMCID: PMCPMC6589685.
7. Murdock DJ, Donoghue PC. Evolutionary origins of animal skeletal biomineralization. Cells Tissues Organs. 2011;194(2-4):98-102. Epub 2011/06/01. doi: 10.1159/000324245. PubMed PMID: 21625061.
8. Knoll AH. Biomineralization and Evolutionary History. Reviews in Mineralogy and Geochemistry. 2003;54:329-56. doi: doi:10.2113/0540329.
9. Gilbert P, Bergmann KD, Boekelheide N, Tambutte S, Mass T, Marin F, et al. Biomineralization: Integrating mechanism and evolutionary history. Sci Adv. 2022;8(10):eabl9653. Epub 20220309. doi: 10.1126/sciadv.abl9653. PubMed PMID: 35263127; PubMed Central PMCID: PMCPMC8906573.
10. Hojo H, McMahon AP, Ohba S. An Emerging Regulatory Landscape for Skeletal Development. Trends Genet. 2016;32(12):774-87. Epub 2016/11/07. doi: 10.1016/j.tig.2016.10.001. PubMed PMID: 27814929; PubMed Central PMCID: PMCPMC5126973.
11. Khor JM, Ettensohn CA. Functional divergence of paralogous transcription factors supported the evolution of biomineralization in echinoderms. eLife. 2017;6. Epub 2017/11/21. doi: 10.7554/eLife.32728. PubMed PMID: 29154754; PubMed Central PMCID: PMCPMC5758115.
12. Fraser GJ, Hulsey CD, Bloomquist RF, Uyesugi K, Manley NR, Streelman JT. An ancient gene network is co-opted for teeth on old and new jaws. PLoS Biol. 2009;7(2):e31. Epub 2009/02/14. doi: 08-PLBI-RA-2652 [pii]

10.1371/journal.pbio.1000031. PubMed PMID: 19215146; PubMed Central PMCID: PMC2637924.
13. Gotliv BA, Addadi L, Weiner S. Mollusk shell acidic proteins: in search of individual functions. Chembiochem : a European journal of chemical biology. 2003;4(6):522-9. Epub 2003/06/10. doi: 10.1002/cbic.200200548. PubMed PMID: 12794863.
14. Gong YU, Killian CE, Olson IC, Appathurai NP, Amasino AL, Martin MC, et al. Phase transitions in biogenic amorphous calcium carbonate. Proc Natl Acad Sci U S A.

793 2012;109(16):6088-93. Epub 2012/04/12. doi: 10.1073/pnas.1118085109. PubMed PMID:
794 22492931; PubMed Central PMCID: PMC3341025.
795 15. Drake JL, Mass T, Haramaty L, Zelzion E, Bhattacharya D, Falkowski PG. Proteomic
796 analysis of skeletal organic matrix from the stony coral Stylophora pistillata. Proc Natl Acad Sci U
797 S A. 2013;110(10):3788-93. Epub 2013/02/23. doi: 10.1073/pnas.1301419110. PubMed PMID:
798 23431140; PubMed Central PMCID: PMCPMC3593878.
799 16. Tucker A, Sharpe P. The cutting-edge of mammalian development; how the embryo
800 makes teeth. Nat Rev Genet. 2004;5(7):499-508. doi: 10.1038/nrg1380. PubMed PMID:
801 15211352.
802 17. Vidavsky N, Addadi S, Schertel A, Ben-Ezra D, Shpigel M, Addadi L, et al. Calcium
803 transport into the cells of the sea urchin larva in relation to spicule formation. Proc Natl Acad Sci
804 U S A. 2016. doi: 10.1073/pnas.1612017113. PubMed PMID: 27791140; PubMed Central PMCID:
805 PMCPMC5111655.
806 18. Bentov S, Brownlee C, Erez J. The role of seawater endocytosis in the biomineralization
807 process in calcareous foraminifera. Proc Natl Acad Sci U S A. 2009;106(51):21500-4. Epub
808 2009/12/17. doi: 10.1073/pnas.0906636106. PubMed PMID: 20007770; PubMed Central
809 PMCID: PMCPMC2799886.
810 19. Kahil K, Varsano N, Sorrentino A, Pereiro E, Rez P, Weiner S, et al. Cellular pathways of
811 calcium transport and concentration toward mineral formation in sea urchin larvae. Proc Natl
812 Acad Sci U S A. 2020;117(49):30957-65. Epub 2020/11/25. doi: 10.1073/pnas.1918195117.
813 PubMed PMID: 33229583; PubMed Central PMCID: PMCPMC7733801.
814 20. Strzelecka-Kiliszek A, Mebarek S, Roszkowska M, Buchet R, Magne D, Pikula S. Functions
815 of Rho family of small GTPases and Rho-associated coiled-coil kinases in bone cells during
816 differentiation and mineralization. Biochim Biophys Acta Gen Subj. 2017;1861(5 Pt A):1009-23.
817 Epub 20170208. doi: 10.1016/j.bbagen.2017.02.005. PubMed PMID: 28188861.
818 21. Golub EE. Role of matrix vesicles in biomineralization. Biochim Biophys Acta.
819 2009;1790(12):1592-8. Epub 20090926. doi: 10.1016/j.bbagen.2009.09.006. PubMed PMID:
820 19786074; PubMed Central PMCID: PMCPMC2783689.
821 22. Lecuit T, Lenne PF, Munro E. Force generation, transmission, and integration during cell
822 and tissue morphogenesis. Annu Rev Cell Dev Biol. 2011;27:157-84. Epub 2011/07/12. doi:
823 10.1146/annurev-cellbio-100109-104027. PubMed PMID: 21740231.
824 23. Munjal A, Lecuit T. Actomyosin networks and tissue morphogenesis. Development.
825 2014;141(9):1789-93. Epub 2014/04/24. doi: 10.1242/dev.091645. PubMed PMID: 24757001.
826 24. Agarwal P, Zaidel-Bar R. Principles of Actomyosin Regulation In Vivo. Trends Cell Biol.
827 2019;29(2):150-63. Epub 2018/11/06. doi: 10.1016/j.tcb.2018.09.006. PubMed PMID:
828 30385150.
829 25. Raftopoulou M, Hall A. Cell migration: Rho GTPases lead the way. Dev Biol.
830 2004;265(1):23-32. doi: 10.1016/j.ydbio.2003.06.003. PubMed PMID: 14697350.
831 26. Miklavc P, Frick M. Actin and Myosin in Non-Neuronal Exocytosis. Cells. 2020;9(6). Epub
832 20200611. doi: 10.3390/cells9061455. PubMed PMID: 32545391; PubMed Central PMCID:
833 PMCPMC7348895.
834 27. Segal D, Zaritsky A, Schejter ED, Shilo BZ. Feedback inhibition of actin on Rho mediates
835 content release from large secretory vesicles. J Cell Biol. 2018;217(5):1815-26. Epub
836 2018/03/03. doi: 10.1083/jcb.201711006. PubMed PMID: 29496739; PubMed Central PMCID:
837 PMCPMC5940311.
838 28. Rousso T, Schejter ED, Shilo BZ. Orchestrated content release from Drosophila glue-
839 protein vesicles by a contractile actomyosin network. Nat Cell Biol. 2016;18(2):181-90. Epub
840 2015/12/08. doi: 10.1038/ncb3288. PubMed PMID: 26641716.

841 29. Langer G, Jan de Nooijer L, Oetjen K. On the role of cytoskeleton in coccolith
842 morphogenesis: the effect of cytoskeleton inhibitors. Journal of Phycology. 2010;46:1252–6. doi:
843 DOI: 10.1111/j.1529-8817.2010.00916.x.
844 30. Durak GM, Brownlee C, Wheeler GL. The role of the cytoskeleton in biomineralisation in
845 haptophyte algae. Scientific reports. 2017;7(1):15409. Epub 2017/11/15. doi: 10.1038/s41598-
846 017-15562-8. PubMed PMID: 29133928; PubMed Central PMCID: PMCPMC5684398.
847 31. Tyszka J, Bickmeyer U, Raitzsch M, Bijma J, Kaczmarek K, Mewes A, et al. Form and
848 function of F-actin during biomineralization revealed from live experiments on foraminifera.
849 Proc Natl Acad Sci U S A. 2019;116(10):4111-6. Epub 2019/02/21. doi:
850 10.1073/pnas.1810394116. PubMed PMID: 30782789; PubMed Central PMCID:
851 PMCPMC6410838.
852 32. Tesson B, Hildebrand M. Dynamics of silica cell wall morphogenesis in the diatom
853 Cyclotella cryptica: substructure formation and the role of microfilaments. J Struct Biol.
854 2010;169(1):62-74. Epub 2009/09/05. doi: 10.1016/j.jsb.2009.08.013. PubMed PMID: 19729066.
855 33. Tesson B, Hildebrand M. Extensive and intimate association of the cytoskeleton with
856 forming silica in diatoms: control over patterning on the meso- and micro-scale. PLoS One.
857 2010;5(12):e14300. Epub 2011/01/05. doi: 10.1371/journal.pone.0014300. PubMed PMID:
858 21200414; PubMed Central PMCID: PMCPMC3000822.
859 34. Qin L, Liu W, Cao H, Xiao G. Molecular mechanosensors in osteocytes. Bone Res.
860 2020;8:23. Epub 20200608. doi: 10.1038/s41413-020-0099-y. PubMed PMID: 32550039;
861 PubMed Central PMCID: PMCPMC7280204.
862 35. Huang X, Chen X, Chen H, Xu D, Lin C, Peng B. Rho/Rho-associated protein kinase
863 signaling pathway-mediated downregulation of runt-related transcription factor 2 expression
864 promotes the differentiation of dental pulp stem cells into odontoblasts. Exp Ther Med.
865 2018;15(5):4457-64. Epub 20180321. doi: 10.3892/etm.2018.5982. PubMed PMID: 29731830;
866 PubMed Central PMCID: PMCPMC5920824.
867 36. Oliveri P, Tu Q, Davidson EH. Global regulatory logic for specification of an embryonic
868 cell lineage. Proc Natl Acad Sci U S A. 2008;105(16):5955-62. Epub 2008/04/17. doi:
869 10.1073/pnas.0711220105. PubMed PMID: 18413610; PubMed Central PMCID: PMC2329687.
870 37. Ettensohn CA, Dey D. KirrelL, a member of the Ig-domain superfamily of adhesion
871 proteins, is essential for fusion of primary mesenchyme cells in the sea urchin embryo. Dev Biol.
872 2017;421(2):258-70. doi: 10.1016/j.ydbio.2016.11.006. PubMed PMID: 27866905.
873 38. Gildor T, Winter MR, Layous M, Hijaze E, Ben-Tabou de-Leon S. The biological regulation
874 of sea urchin larval skeletogenesis - From genes to biomineralized tissue. J Struct Biol.
875 2021:107797. Epub 2021/09/17. doi: 10.1016/j.jsb.2021.107797. PubMed PMID: 34530133.
876 39. Vidavsky N, Addadi S, Mahamid J, Shimoni E, Ben-Ezra D, Shpigel M, et al. Initial stages
877 of calcium uptake and mineral deposition in sea urchin embryos. Proc Natl Acad Sci U S A.
878 2014;111(1):39-44. Epub 2013/12/18. doi: 10.1073/pnas.1312833110. PubMed PMID:
879 24344263; PubMed Central PMCID: PMC3890786.
880 40. Wilt FH, Killian CE, Hamilton P, Croker L. The dynamics of secretion during sea urchin
881 embryonic skeleton formation. Exp Cell Res. 2008;314(8):1744-52. Epub 2008/03/22. doi:
882 10.1016/j.yexcr.2008.01.036. PubMed PMID: 18355808; PubMed Central PMCID: PMC2444014.
883 41. Adomako-Ankomah A, Ettensohn CA. Growth factor-mediated mesodermal cell
884 guidance and skeletogenesis during sea urchin gastrulation. Development. 2013;140(20):4214-
885 25. doi: 10.1242/dev.100479. PubMed PMID: 24026121.
886 42. Morgulis M, Gildor T, Roopin M, Sher N, Malik A, Lalzar M, et al. Possible cooption of a
887 VEGF-driven tubulogenesis program for biomineralization in echinoderms. Proc Natl Acad Sci U S
888 A. 2019. doi: 10.1073/pnas.1902126116. PubMed PMID: 31152134.

889 43. Sun Z, Ettensohn CA. Signal-dependent regulation of the sea urchin skeletogenic gene
890 regulatory network. Gene Expr Patterns. 2014;16(2):93-103. doi: 10.1016/j.gep.2014.10.002.
891 PubMed PMID: 25460514.
892 44. Tarsis K, Gildor T, Morgulis M, Ben-Tabou de-Leon S. Distinct regulatory states control
893 the elongation of individual skeletal rods in the sea urchin embryo. Dev Dyn. 2022. Epub
894 20220410. doi: 10.1002/dvdy.474. PubMed PMID: 35403290.
895 45. Morgulis M, Winter MR, Shternhell L, Gildor T, Ben-Tabou de-Leon S. VEGF signaling
896 activates the matrix metalloproteinases, MmpL7 and MmpL5 at the sites of active skeletal
897 growth and MmpL7 regulates skeletal elongation. Dev Biol. 2021;473:80-9. Epub 2021/02/13.
898 doi: 10.1016/j.ydbio.2021.01.013. PubMed PMID: 33577829.
899 46. Winter MR, Morgulis M, Gildor T, Cohen AR, Ben-Tabou de-Leon S. Calcium-vesicles
900 perform active diffusion in the sea urchin embryo during larval biomineralization. PLoS Comput
901 Biol. 2021;17(2):e1008780. Epub 2021/02/23. doi: 10.1371/journal.pcbi.1008780. PubMed
902 PMID: 33617532; PubMed Central PMCID: PMCPMC7932551.
903 47. Stepicheva NA, Dumas M, Kobi P, Donaldson JG, Song JL. The small GTPase Arf6
904 regulates sea urchin morphogenesis. Differentiation. 2017;95:31-43. doi:
905 10.1016/j.diff.2017.01.003. PubMed PMID: 28188999.
906 48. Moreno B, DiCorato A, Park A, Kellen Mobilia, Knapp R, Bleher R, et al. Culture of and
907 experiments with sea urchin embryo primary mesenchyme cells. Methods in Cell Biology.
908 2019;150:293-330.
909 49. Sepulveda-Ramirez SP, Toledo-Jacobo L, Henson JH, Shuster CB. Cdc42 controls primary
910 mesenchyme cell morphogenesis in the sea urchin embryo. Dev Biol. 2018;437(2):140-51. Epub
911 2018/03/21. doi: 10.1016/j.ydbio.2018.03.015. PubMed PMID: 29555242; PubMed Central
912 PMCID: PMCPMC5973877.
913 50. Croce J, Duloquin L, Lhomond G, McClay DR, Gache C. Frizzled5/8 is required in
914 secondary mesenchyme cells to initiate archenteron invagination during sea urchin
915 development. Development. 2006;133(3):547-57. doi: 10.1242/dev.02218. PubMed PMID:
916 16396908.
917 51. Ettensohn CA, McClay DR. Cell lineage conversion in the sea urchin embryo. Dev Biol.
918 1988;125(2):396-409. Epub 1988/02/01. doi: 10.1016/0012-1606(88)90220-5. PubMed PMID:
919 3338620.
920 52. Chen W, Mao K, Liu Z, Dinh-Xuan AT. The role of the RhoA/Rho kinase pathway in
921 angiogenesis and its potential value in prostate cancer (Review). Oncol Lett. 2014;8(5):1907-11.
922 Epub 20140821. doi: 10.3892/ol.2014.2471. PubMed PMID: 25289078; PubMed Central PMCID:
923 PMCPMC4186560.
924 53. Jacobs M, Hayakawa K, Swenson L, Bellon S, Fleming M, Taslimi P, et al. The structure of
925 dimeric ROCK I reveals the mechanism for ligand selectivity. J Biol Chem. 2006;281(1):260-8. doi:
926 10.1074/jbc.M508847200. PubMed PMID: 16249185.
927 54. Liu J, Wada Y, Katsura M, Tozawa H, Erwin N, Kapron CM, et al. Rho-Associated Coiled-
928 Coil Kinase (ROCK) in Molecular Regulation of Angiogenesis. Theranostics. 2018;8(21):6053-69.
929 Epub 2019/01/08. doi: 10.7150/thno.30305. PubMed PMID: 30613282; PubMed Central PMCID:
930 PMCPMC6299434.
931 55. Julian L, Olson MF. Rho-associated coiled-coil containing kinases (ROCK): structure,
932 regulation, and functions. Small GTPases. 2014;5:e29846. Epub 2014/07/11. doi:
933 10.4161/sgtp.29846. PubMed PMID: 25010901; PubMed Central PMCID: PMCPMC4114931.
934 56. Amin E, Dubey BN, Zhang SC, Gremer L, Dvorsky R, Moll JM, et al. Rho-kinase:
935 regulation, (dys)function, and inhibition. Biol Chem. 2013;394(11):1399-410. doi: 10.1515/hsz-
936 2013-0181. PubMed PMID: 23950574; PubMed Central PMCID: PMCPMC5538733.

937 57. Pavlov D, Muhlrad A, Cooper J, Wear M, Reisler E. Actin filament severing by cofilin. J
938 Mol Biol. 2007;365(5):1350-8. Epub 20061103. doi: 10.1016/j.jmb.2006.10.102. PubMed PMID:
939 17134718; PubMed Central PMCID: PMCPMC2572264.
940 58. Yarmola EG, Somasundaram T, Boring TA, Spector I, Bubb MR. Actin-latrunculin A
941 structure and function. Differential modulation of actin-binding protein function by latrunculin
942 A. J Biol Chem. 2000;275(36):28120-7. doi: 10.1074/jbc.M004253200. PubMed PMID: 10859320.
943 59. Schatten G, Schatten H, Spector I, Cline C, Paweletz N, Simerly C, et al. Latrunculin
944 inhibits the microfilament-mediated processes during fertilization, cleavage and early
945 development in sea urchins and mice. Exp Cell Res. 1986;166(1):191-208. doi: 10.1016/0014-
946 4827(86)90519-7. PubMed PMID: 3743654.
947 60. Kovacs M, Toth J, Hetenyi C, Malnasi-Csizmadia A, Sellers JR. Mechanism of blebbistatin
948 inhibition of myosin II. J Biol Chem. 2004;279(34):35557-63. Epub 20040616. doi:
949 10.1074/jbc.M405319200. PubMed PMID: 15205456.
950 61. Moorhouse KS, Gudejko HF, McDougall A, Burgess DR. Influence of cell polarity on early
951 development of the sea urchin embryo. Dev Dyn. 2015;244(12):1469-84. Epub 20150925. doi:
952 10.1002/dvdy.24337. PubMed PMID: 26293695; PubMed Central PMCID: PMCPMC4715636.
953 62. Mabuchi I. Cleavage furrow: timing of emergence of contractile ring actin filaments and
954 establishment of the contractile ring by filament bundling in sea urchin eggs. J Cell Sci. 1994;107
955 (Pt 7):1853-62. doi: 10.1242/jcs.107.7.1853. PubMed PMID: 7983152.
956 63. Schroeder TE. Fourth cleavage of sea urchin blastomeres: microtubule patterns and
957 myosin localization in equal and unequal cell divisions. Dev Biol. 1987;124(1):9-22. doi:
958 10.1016/0012-1606(87)90454-4. PubMed PMID: 3311851.
959 64. Wong GK, Allen PG, Begg DA. Dynamics of filamentous actin organization in the sea
960 urchin egg cortex during early cleavage divisions: implications for the mechanism of cytokinesis.
961 Cell motility and the cytoskeleton. 1997;36(1):30-42. doi: 10.1002/(SICI)1097-
962 0169(1997)36:1<30::AID-CM3>3.0.CO;2-L. PubMed PMID: 8986375.
963 65. Khor JM, Ettensohn CA. Transcription Factors of the Alx Family: Evolutionarily Conserved
964 Regulators of Deuterostome Skeletogenesis. Frontiers in genetics. 2020;11:569314. Epub
965 2020/12/18. doi: 10.3389/fgene.2020.569314. PubMed PMID: 33329706; PubMed Central
966 PMCID: PMCPMC7719703.
967 66. Bond LM, Brandstaetter H, Sellers JR, Kendrick-Jones J, Buss F. Myosin motor proteins
968 are involved in the final stages of the secretory pathways. Biochem Soc Trans. 2011;39(5):1115-
969 9. doi: 10.1042/BST0391115. PubMed PMID: 21936774; PubMed Central PMCID:
970 PMCPMC3403808.
971 67. Bibeau JP, Kingsley JL, Furt F, Tuzel E, Vidali L. F-Actin Mediated Focusing of Vesicles at
972 the Cell Tip Is Essential for Polarized Growth. Plant Physiol. 2018;176(1):352-63. Epub 20171002.
973 doi: 10.1104/pp.17.00753. PubMed PMID: 28972078; PubMed Central PMCID:
974 PMCPMC5761772.
975 68. Olson EN, Nordheim A. Linking actin dynamics and gene transcription to drive cellular
976 motile functions. Nat Rev Mol Cell Biol. 2010;11(5):353-65. Epub 2010/04/24. doi:
977 10.1038/nrm2890. PubMed PMID: 20414257; PubMed Central PMCID: PMCPMC3073350.
978 69. Knipe RS, Tager AM, Liao JK. The Rho kinases: critical mediators of multiple profibrotic
979 processes and rational targets for new therapies for pulmonary fibrosis. Pharmacol Rev.
980 2015;67(1):103-17. doi: 10.1124/pr.114.009381. PubMed PMID: 25395505; PubMed Central
981 PMCID: PMCPMC4279074.
982 70. Khatiwala CB, Kim PD, Peyton SR, Putnam AJ. ECM compliance regulates osteogenesis by
983 influencing MAPK signaling downstream of RhoA and ROCK. J Bone Miner Res. 2009;24(5):886-

984 98. doi: 10.1359/jbmr.081240. PubMed PMID: 19113908; PubMed Central PMCID:
985 PMCPMC2672206.
986 71. Zhong J, Yang Y, Liao L, Zhang C. Matrix stiffness-regulated cellular functions under
987 different dimensionalities. Biomater Sci. 2020;8(10):2734-55. Epub 20200423. doi:
988 10.1039/c9bm01809c. PubMed PMID: 32322859.
989 72. Luo YJ, Su YH. Opposing nodal and BMP signals regulate left-right asymmetry in the sea
990 urchin larva. PLoS Biol. 2012;10(10):e1001402. Epub 2012/10/12. doi:
991 10.1371/journal.pbio.1001402. PubMed PMID: 23055827; PubMed Central PMCID:
992 PMC3467216.
993 73. Stalling D, Westerhoff M, Hege H-C. Amira: A highly interactive system for visual data
994 analysis. The visualization handbook. 2005;38:749-67.

995